

## **Assessment of PWT Conditions for the STARDUST Post-Flight Evaluation**

R. Wernitz, M. Fertig, G. Herdrich, S. Löhle, M. Winter, H.-P. Röser

Institut für Raumfahrtssysteme (IRS), Universität Stuttgart,  
Pfaffenwaldring 31, D-70569 Stuttgart

### **ABSTRACT**

On January 15th 2006, the STARDUST capsule re-entered Earth's atmosphere after its almost seven year journey with a re-entry speed of 12.8 km/s. Data on heat shield erosion and plasma characterization is considered to be very valuable for the vehicle design for further missions since the entry conditions are typical for hyperbolic re-entries for sample return missions e.g. from Mars.

During an observation mission aboard the NASA DC-8 airborne observatory the SLIT experiment was conducted. Here, a conventional spectrometer in a Cerny Turner configuration was fed by fiber optics with light collected by a small mirror telescope. Data was taken during 30 s around peak heating until the capsule left the accessible observation region. The emission of CN as a major erosion product of the PICA (Phenolic Impregnated Carbon Ablator) heat shield material as well as  $N_2^+$  and different atoms could be monitored successfully during that time. Planck temperatures as well as rotational and vibrational temperatures of CN and  $N_2^+$  were extracted along the visible trajectory.

The paper provides a short summary of the obtained spectra for different flight altitudes of STARDUST. Furthermore a comparison to the results of numerical simulations of the plasma emission with PARADE and URANUS radiation / flow field simulations will be presented.

In order to further interpret the obtained data, ground testing at the IRS plasma wind tunnels (PWT) is required. Thus, suitable measurement techniques for testing must be selected, essentially including emission spectroscopy in order to facilitate plasma characterization and consequently the comparability of PWT experimental results to the data obtained during STARDUST observation.

Furthermore, testing conditions are identified and assessed. Here, constant surface heat flux is chosen as a general testing condition in a first approach. In addition, different ablative materials for testing are selected, starting with graphite as a basic material and including if possible the original PICA TPS or else, similar materials.

## 1.0 Introduction

The flight of the STARDUST capsule which performed the fastest re-entry ever is considered as a prototype mission for future hyperbolic re-entry missions as e.g. sample return from Mars. Figure 1 shows the expected loads determined from trajectory data<sup>6</sup>.

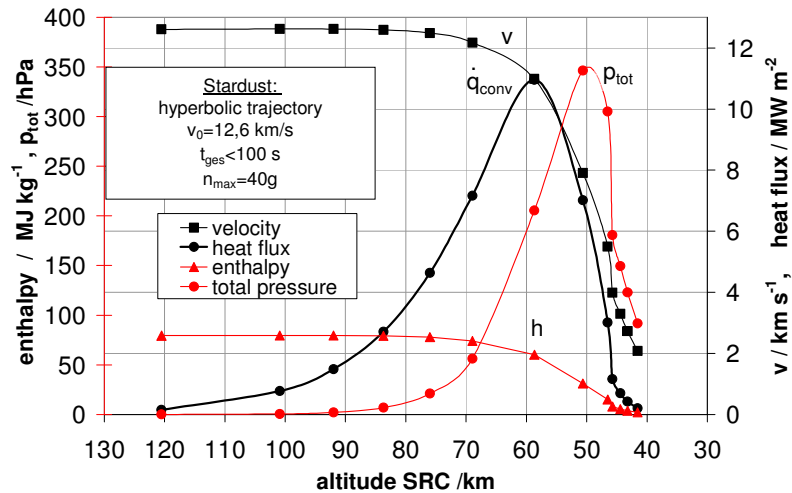


Figure 1: STARDUST trajectory

For the re-entry phase, no diagnostics were installed on the capsule. Therefore, information on heat shield and re-entry plasma was obtained by passive optical methods aboard the NASA DC-8 airborne observatory [1] mission. Detection of radiation below 300 nm was impossible though, due to the ozone layer at altitudes between 25 km and 50 km. Experiments by American, Japanese and German researchers included spectrally resolved set-ups using transmission gratings and a mini Echelle spectrometer [7] [8].

The German SLIT experiment made use of a conventional spectrometer in a Cerny Turner configuration ( $f=300\text{mm}$ , grating  $600\text{ l/mm}$ ) fed by fiber optics, where measured values are an integration both over the visible part of the heat shield and the plasma in the post shock region. The spectra therefore contain a superposition of continuum spectra (heat shield radiation and continuum radiation of dust particles in the plasma) and line spectra from the plasma in the post shock layer, which must be separated during evaluation.

The capsule was tracked manually, which was a major challenge since the angle of vision of the telescope was limited to 0.45 degrees focused on the fiber optics. Data was taken during 30 s with a measurement frequency of 5 Hz around peak heating until the capsule left the observed region. Due to the difficulties in tracking not every spectrum contained data.

The choice of a spectrometer with an entrance slit provided a fixed wavelength range for the observation. Thus, SLIT provided both spectral data at fairly high spectral resolution and a spectral benchmark for the transmission grating measurements.

The set-up will be described in more detail. Furthermore, an evaluation of the experimental data is presented, including the calibration of the setup, the separation of continuum and line spectra and the interpretation of both spectra with respect to Planck temperatures taken from the continuum spectra.

Finally, PWT conditions for the rebuilding of the STARDUST re-entry are identified and the STARDUST heat flux at peak heating is reproduced experimentally.

## 2.0 Experimental Setup of SLIT

The experimental setup is shown in Figure 2, including telescope, fiber optics and spectrometer.

An Acton 300i lab spectrometer (300 mm focal length) was connected to an Andor DU971N EMCCD camera with 1600x400 pixels (16x16  $\mu\text{m}$  each) for detection. The measurement was conducted with a grating of  $600 \text{ mm}^{-1}$  at wavelengths from 324 nm to 456 nm. The pixel resolution was 0.08 nm, the *FWHM* of the measurement was 0.3 nm.

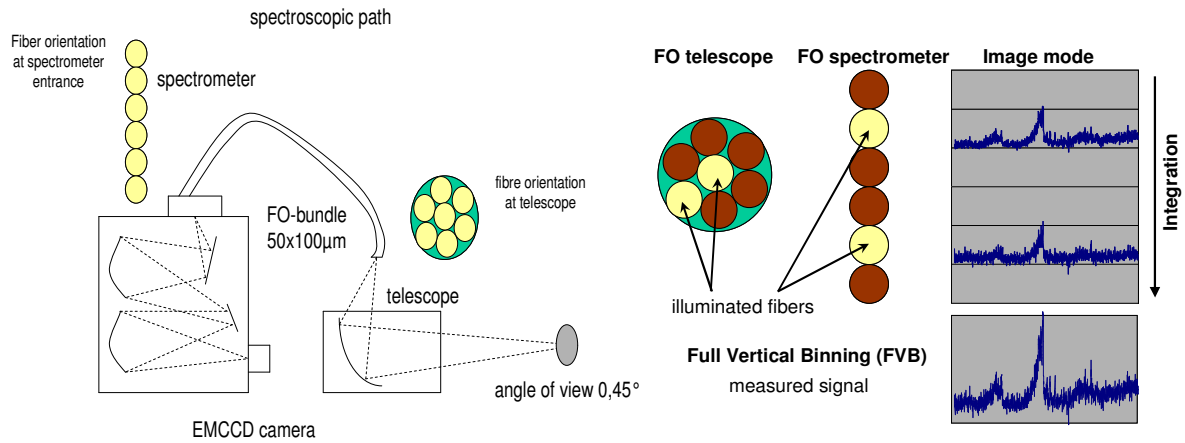


**Figure 2: Experimental setup (left) and full vertical binning (right)**

The  $f/d$  ratio of the optics was limited to roughly 2 by the fiber optics numerical aperture of  $n_a=0.22$ .

The reflector telescope, used for focusing on STARDUST, included an off-axis parabolic mirror (100 mm equivalent focal length, 50 mm diameter) and was connected to the spectrometer via fiber optics of 50 fibers at 100  $\mu\text{m}$  diameter (each fiber). The fibers attached to the telescope exit were of circular configuration at 0.6 mm diameter and an angle of vision of  $0.45^\circ$ . At the spectrometer entrance the fibers were reoriented into a straight line forming an entrance slit of less than 100  $\mu\text{m}$  effective slit width.

Individual fibers of the circular cross section were not assigned to their position at the spectrometer slit due to manufacture. Therefore, data was acquired via full vertical binning, meaning that all CCD columns were integrated and displayed as a single spectrum, see Figure 2. This approach generally reduces noise, furthermore, the signal to noise ratio is improved.

Since the angle of vision of  $0.45^\circ$  was far too small for manual tracking, a video camera combined with a light intensifier with a Canon lens system (focal length 100 mm,  $f/2.0$ ) with a viewing angle of roughly  $20^\circ$  was used. The intensifier was rigidly connected to the mount of the telescope guaranteeing a defined relation between the viewing angles of the camera and the telescope/ spectrometer.

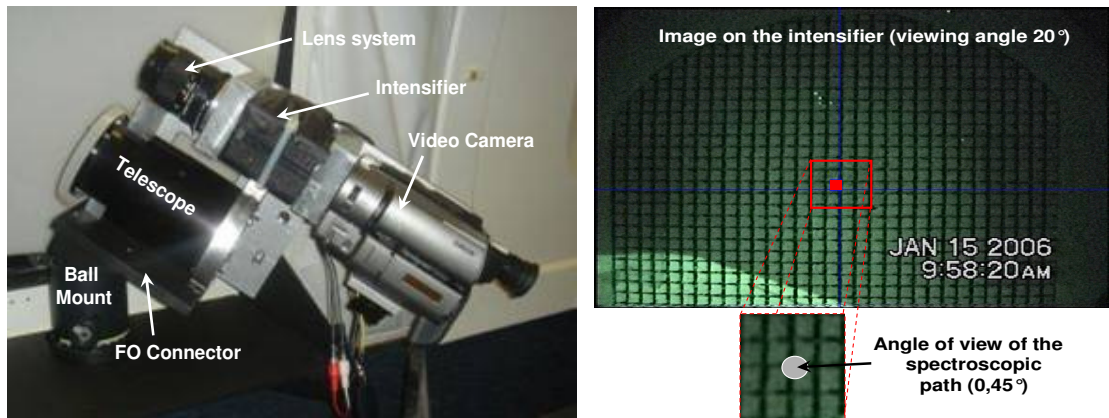


**Figure 3: Left: Video camera – intensifier combination and telescope mounted on the base plate; Right: Angle of vision of the telescope as seen on the video image**

Figure 3 shows the combined set-up mounted on a ball mount at the window of the airplane. A grid was glued to the intensifier screen which facilitated assignment of the detected spot on the video to the spectrometer-telescope combination. The red dot in Figure 3 demonstrates the area detected by the spectrometer. This area was determined before flight by taking images of the moon, whose angle of vision is roughly equal to that of the fiber optics of  $0.45^\circ$ .

The reentry was observed during 30 s starting at altitudes of 84 km down to roughly 45 km. The acquisition time of the spectra was 0.2 s at a repetition frequency of 5 Hz. Due to difficulties in manual tracking not every spectrum contained data. Consequently, the overall intensity showed fluctuations, too, when the fiber bundle was only partly illuminated. Therefore, only spectra of maximum intensity were used to obtain absolute intensity information.

Additionally, some measurements show the plasma wake behind the capsule. These spectra may provide information on ablation products in the plasma.

Despite the rigid fixation of telescope and intensifier, the video camera still moved slightly. The slight movements of the video image resulting from this were taken into account during evaluation.

### 3.0 Data correction, calibration and data allocation

Experimental data must be corrected for background and cosmic rays. Time and the section of the capsule, i.e. stagnation point or wake, must be determined. The spectral data was wavelength corrected and intensity calibrated. Atmospheric absorption must be taken into account, which requires calculating the distance to the capsule and its orientation towards the airplane.

#### Correction for background and cosmic rays

The intensity of cosmic rays in the spectra is of similar magnitude as the plasma emission lines, due to the high sensitivity and amplification of the camera. The lines appear on one single camera pixel and thus are much narrower than plasma emission lines which are broadened by optical components to a FWHM of 4 pixels.

Furthermore pixel 997 (406.6 nm wavelength) had to be eliminated from the spectra, since it yielded an abnormally high intensity of approximately 10 times the usual plasma emission intensity, see Figure 4 (“hot pixel column”).

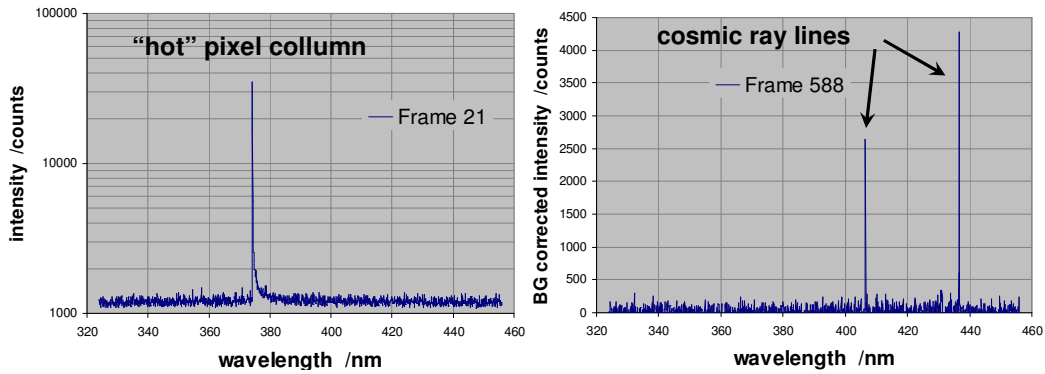


**Figure 4: Correction for cosmic rays and pixel 997**

Due to the position of the video camera not being perfectly still towards the telescope, the position of the capsule on the video images does not correspond to a fixed point on the CCD array, as mentioned above. This movement therefore had to be compensated using a C routine, where groups of pixels were defined, their intensity integrated and displayed vs. time. This intensity distribution was compared to the total intensity of the spectra, i.e. the sum over all pixels. The resulting area (pixels) on the video, which corresponds to the measurement position, gives information on the section of the capsule captured (i.e. stagnation point, wake), see Figure 5. Note that a perfect match can not be expected because the intensity of the video image is falsified by absorption due to the lines of the grid.

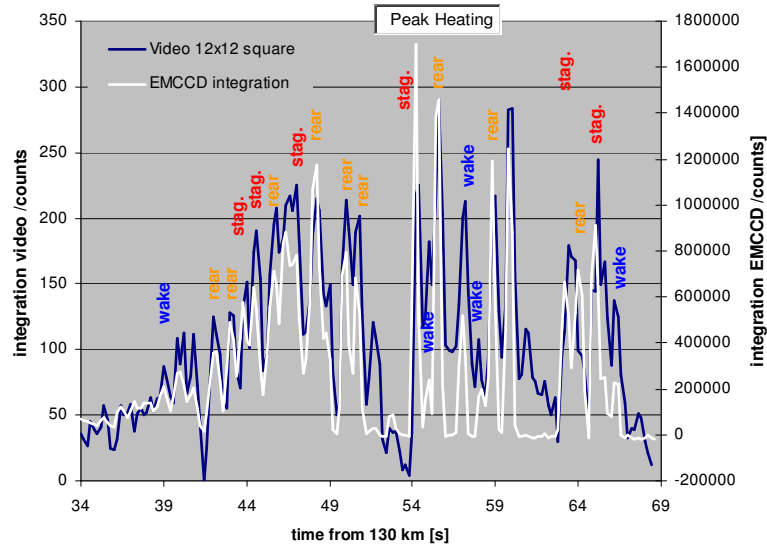


**Figure 5: Sections of the capsule corresponding to the measured spectra**

### Wavelength and Intensity Calibration

Wavelength calibration was performed by measuring the emission of a Mercury lamp and using a second order polynomial fit.

For intensity calibration, an Ocean Optics calibration lamp was placed ( $L_{\text{lamp-telescope}} = 3.86$  m) from the telescope. For the calibration radiant power was used rather than radiance, since the distance to the capsule (440 km to 70 km) obviously can not be reproduced during calibration and furthermore the solid angle of the capsule and atmospheric transmission varied during the re-entry observation.

The intensity  $I_{O-O}$  using an optical fiber connected directly to the lamp port was given in  $\mu\text{W}/(\text{cm}^2 \text{ cm})$ . This intensity was converted to spectral radiance using the numerical aperture of a typical fiber of  $n_a = 0.22$ . The calibration values were transformed to radiant power at the entrance of the telescope using the

distance between lamp and telescope in combination with the telescope aperture diameter. Finally, this value was integrated over the wavelength interval covered by each pixel.

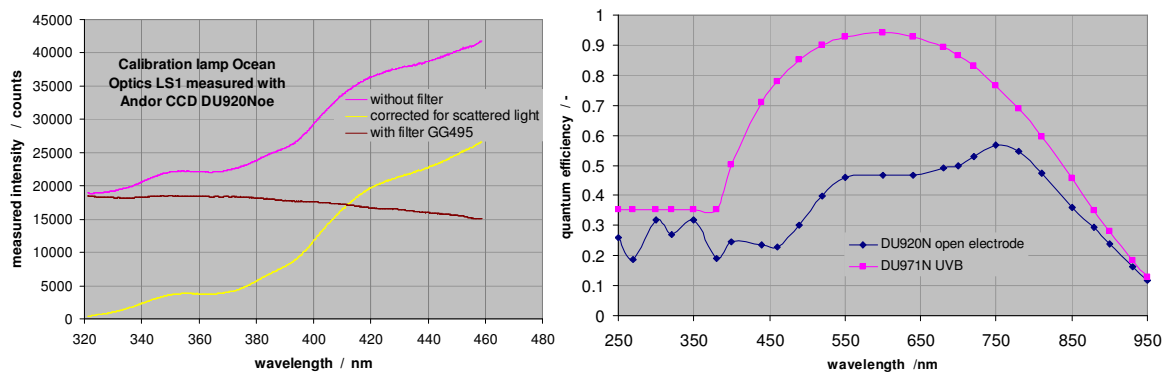
Discrepancies between calibrated and simulated spectra called for recalibration with respect to scattered light, since the calibration lamp emits in the visible and near IR range while the experiment's wavelength range is the UV. This IR radiation (of the calibration lamp) causes scattering in the telescope and thus on the CCD.

Figure 6 shows the intensity of a similar calibration lamp (Ocean Optics LS1) with and without edge filter (Schott GG495) blocking the radiation of the measured range. The difference between the two intensities gives the lamp emission corrected for scattered light.

The Andor DU971N UVB EMCCD camera which was used during the observation mission was not available for recalibration. Therefore, an Andor DU920N was used, since the dimensions of its CCD chip are equal to those of the Andor DU971N UVB.

The amount of scattered radiation depends on the spectrometer, the grating and the fiber optics (which were not changed). Since the spectral quantum efficiencies of the two cameras are substantially different, as shown in Figure 6, the spectral composition of the scattered light and therefore its position on the CCD array (corresponding to the wavelength) are unknown for wavelengths different to the calibration lamp's range of 320 nm to 460 nm.

Therefore, measurements with a series of edge filters (edges at 495 nm, 515 nm, 535 nm, 550 nm, 570 nm, 590 nm, 610 nm, 630 nm, 645 nm, 665 nm, 695 nm, 715 nm, 780 nm, 830 nm and 850 nm) were conducted in order to estimate the spectral composition of the scattered light. The main effects were found for radiation of 600 nm to 850 nm.



**Figure 6: Ocean Optics LS1 measured with Andor DU920N open electrode with and without edge filter GG495 (left) and quantum efficiencies of Andor DU971N UVB and Andor DU920N (right).**

Since the quantum efficiencies of both the DU920N and the DU971N are known, measurements may be converted to the DU971N, using a factor, which yields the scattered light as a portion of the original calibration measurement. Furthermore, to obtain sufficient agreement between the original calibration and the recalibration based on the quantum efficiency data, the amount of scattered light had to be increased by 20%. Figure 7 gives the calibration factors with and without correction for scattered light as well as the calibrated curve provided by Ocean Optics.

The thermal emission of the heat shield qualitatively shows a similar characteristic as the calibration lamp meaning that the continuous thermal radiation will also produce scattering. Furthermore, the amount of scattered light depends on the spectral distribution in the VIS and NIR range. Thus a black body source in combination with the edge filters described above was used to estimate the amount and distribution of scattering due to Planck emission using the same method as explained above.

Figure 8 shows scattered light and wanted signal (of the black body source) in the temperature range concerned normalized with maximum signal (i.e. at the highest wavelength). It is obvious that the portion of scattered light varies with Planck temperature. At low temperatures, the signal of the black body source is almost zero. The portion of the signal due to the black body does not exceed 10%.

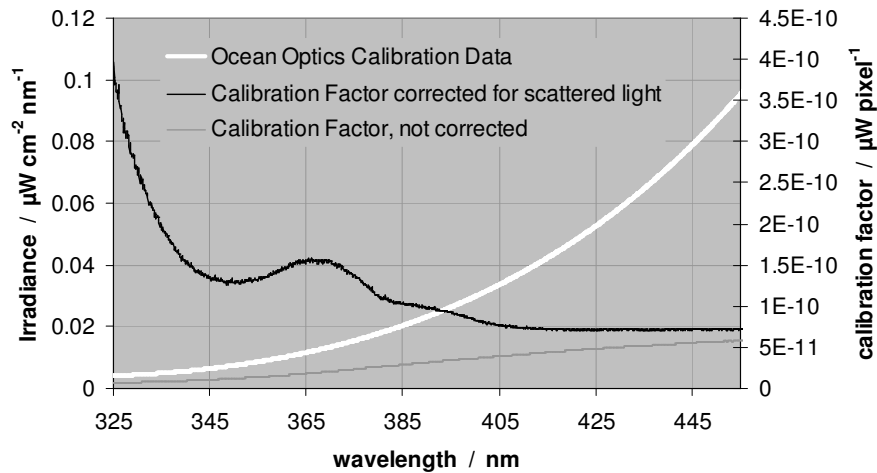


**Figure 7: SLIT calibration factor with / out scattering**

Therefore, each spectrum of scattered light must be treated individually.

As the EMCCD camera (DU971N) was unavailable, the plasma spectra obtained using original (wrong) calibration factors were recalibrated using the ratio of the two calibration factors (with / out corrections for scattered light), as a first approach.

For the thermal emission, a uniform calibration was not possible since the underlying Planck temperatures are not known, requiring an iterative process. Rather than converting the measured signal to radiant power, the simulated Planck emission of the capsule was converted to counts measured by the spectrometer system. Therefore, a Planck temperature distribution was fitted to the spectrum, thus obtaining Planck temperatures via the best fit. This thermal emission is discussed below in more detail.

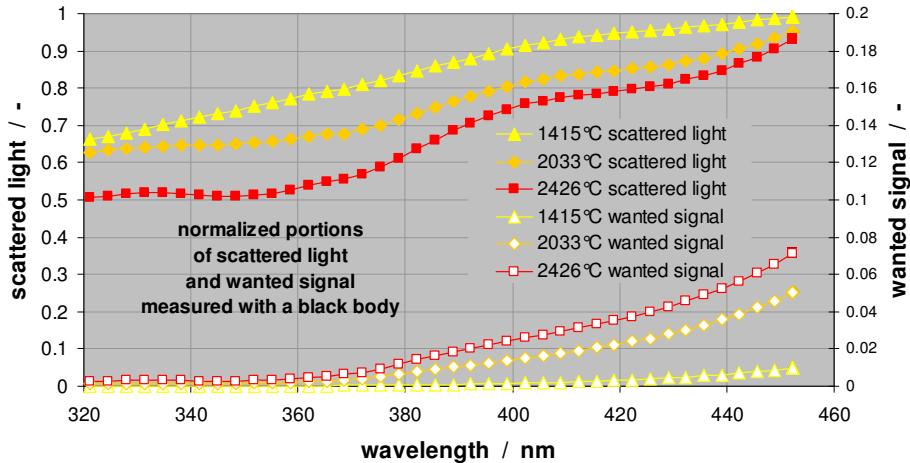


**Figure 8: Scattered light (Planck radiation) obtained with a black body source at different temperatures**

### Atmospheric Transmission

In order to obtain the radiation of the capsule from the experimental data one has to consider its solid angle, which depends on its distance to the airplane, its surface area (or the emitting plasma volume) and, additionally, the atmospheric transmission. The spectral transmission of the atmosphere was computed using the ModTran code [9]. The aerosole concentration was assumed to be “normal”, while the ozone concentration was taken from ozone maps, see Figure 9.



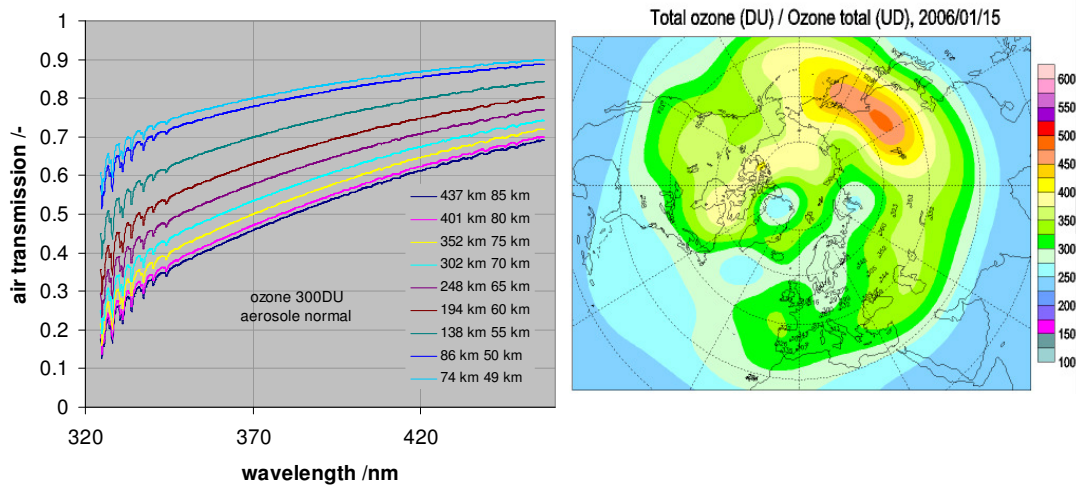


**Figure 9: Atmospheric transmission between DC8 and Stardust for different Stardust altitudes and ozone map for 2006/01/15 from [10]**

#### 4.0 Evaluation and interpretation

Generally, the observed spectra are a superposition of the post shock plasma radiation and continuous radiation of the heat shield. In order to simplify the evaluation, both the plasma parameters and the heat shield temperature are considered to be constant. Ablation particles injected into the flow also emit continuum radiation due to their temperature. Improvements to the evaluation procedure concerning these simplifications are discussed below.

At first the plasma and Planck radiation must be separated. To quantify the Planck radiation, the visible surface of the Stardust capsule and its orientation towards the airplane (i.e. the angle of the surface normal vector and the flight direction of the airplane) must be calculated.

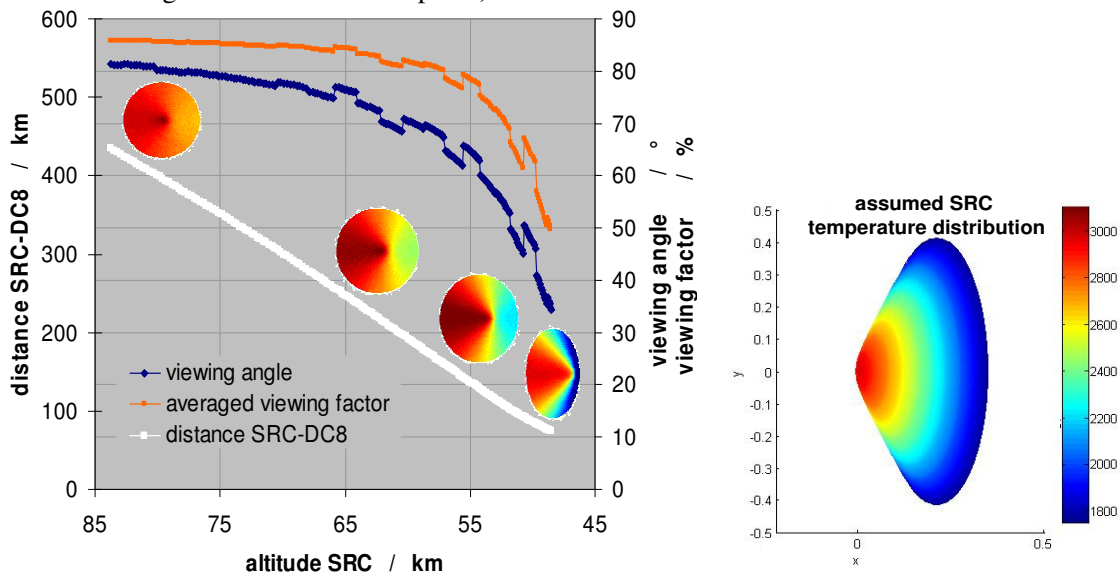


**Figure 10: View factor, angle of vision and distance to capsule: The color of the capsule's surface indicates the local view factors along the trajectory (red~1, blue~0.2) (left) and heat shield temperature distribution (right)**



### Visible Surface and View Factors

The position and orientation of the DC8 is known from GPS data, while the Stardust position is taken from trajectory data. The capsule's axis is assumed to be oriented in the direction of the velocity vector which for each altitude is the difference of two subsequent trajectory points, see Figure 10. Here, the angle of vision is  $90^\circ$  if the observation axis is parallel to the capsule's axis (front) and  $0^\circ$  if the vehicle is observed rectangular to its flight vector (side). The minimum angle during the observation was  $34.33^\circ$  at 48.5 km altitude. The surface was calculated as a sphere with 0.22 m radius connected tangentially to a truncated cone of  $30.5^\circ$  with 0.405 m outer radius, i.e. the entire heat shield ( $0.5947 \text{ m}^2$ ) was visible up to  $30.5^\circ$  angle of vision.

According to Lambert's Law the detected intensity of a radiating surface is proportional to the cosine of the angle of vision. Therefore, the detected intensities decrease with this angle, seemingly yielding an increase of the Planck temperature. This effect is remedied calculating the view factor.

For constant surface temperature, an integration over the surface yields an averaged view factor for each altitude as depicted in Figure 10. For any other temperature distribution, one must integrate the product of the locally emitted Planck radiation and the view factor.

### Heat Shield Temperatures

As a simplification, a linear temperature distribution along the axis was assumed. Spectral heat shield radiance is calculated using Planck's formula for grey bodies:

$$M_\lambda(T) = \frac{\epsilon_\lambda 2\pi hc^2}{\lambda^5} \frac{1}{\exp(hc/\lambda kT) - 1}$$

The emissivity of PICA is assumed to be independent of  $\lambda$ , since no spectral data is available. Furthermore, a temperature dependency of  $\epsilon$  was assumed according to [11] for temperatures up to 1900K from 0.8 to 0.9. The data applies for charred PICA (rather than virgin material).

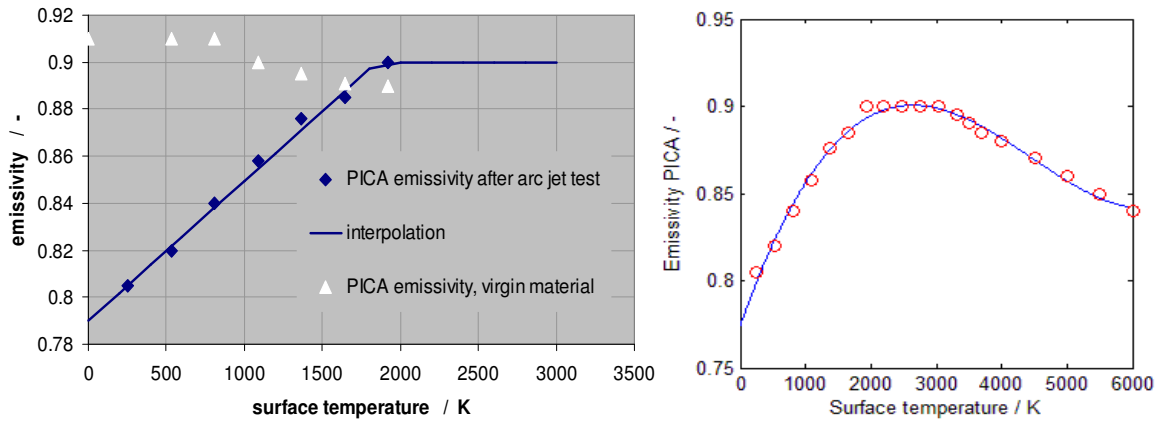


Figure 11: Emissivity of PICA: Data (left) and interpolation (right)

The spectral radiance is integrated to the wavelengths of the CCD pixels and then multiplied by the visible surface area, the atmospheric transmission and the solid angle,

$$\Omega = 2\pi(1 - \cos \alpha), \quad \frac{\alpha}{2} = \arctan\left(\frac{D_{tel}}{2L_{Capsule-DC8}}\right),$$

where the half apex angle is calculated using the aperture diameter of the telescope  $D_{tel}$  and the distance between STARDUST and the DC8  $L_{Capsule-DC8}$ . Thus, the radiant power at the entrance aperture of the telescope is:

$$\Phi = \int_{\Delta\lambda_{pixel}} M_\lambda \Omega A_{vis} \tau_{atm} \Delta\lambda_{pixel}$$

For the linear temperature distribution along the heat shield, the temperature at the edge of the cone was set to 1750 K, while the stagnation point temperature was varied, see Figure 10. The emitted radiation was then calculated by integrating over the surface area, taking into account the angle of vision, and multiplied by the solid angle of detection and the air transmission. The peak temperatures obtained are considered an upper limit, since ablation particles in the plasma layer have not been taken into account.

For further interpretation, a parametric variation of the bottom temperature and temperature distributions other than linear ones are presently implemented. Additionally, particle radiation should be taken into account.

Moreover, due to the calibration issues discussed above, scattered light must be taken into account. Using recalibration as described in section 3.0, in particular using a black body source at different temperatures in the range of expected surface temperatures, requires an iterative process, since the emission temperature must be known to choose the correct calibration function. The STARDUST surface temperature distribution further complicates matters. Nevertheless, these measurements might prove very helpful to more accurately determine the sensitivity of the set-up with respect to the spectral distribution of scattered light.

The sensitivity of the set-up to scattered light was determined from the calibration measurements described in section 3 as a simplification. The measured spectrum was rebuilt based on the spectral distribution of the calibration lamp.

Figure 12 shows the Planck radiation and the resulting plasma spectrum (which is the difference between measurement and Planck) at 56.79 km of altitude. Here, the Planck radiation was determined for two stagnation point temperatures. The lower temperature curve was fitted to the spectrum at shorter wavelengths. For high wavelengths, the Planck radiation was calculated for the higher peak temperature. This phenomenon is probably due to the linear temperature distribution being inaccurate or an over-prediction of scattered light at small wavelengths, due to the low sensitivity at these wavelengths.

Determining Planck temperatures at different altitudes one obtains the peak surface temperature of the capsule along its flight trajectory, see Figure 12.

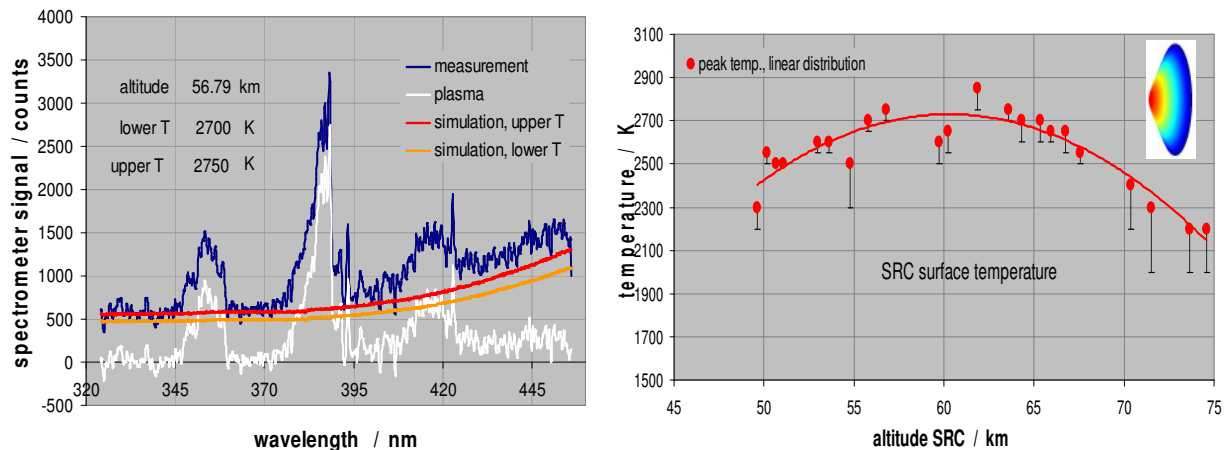


**Figure 12: Measurement (blue) spectrum and spectrum corrected for Planck radiation at two stagnation point temperatures (left) and stagnation point temperatures obtained from Planck radiation using linear surface temperature distribution**

### Evaluation of plasma spectra

The emission spectra are dominated by the emission of CN and  $N_2^+$ . Atomic lines are seen; the emission of Ca and  $C^+$  was clearly identified and strong evidence was found for the appearance of H, C and  $O^+$ . Possibly O and N are present, whereas  $N^+$  lines are missing, see Figure 15.

A numerical simulation of the molecular radiation of CN and  $N_2^+$  was carried out varying the rotational and vibrational temperatures from 1000 K to 15000 K. These temperatures define the band shape of the

molecular bands and therefore may be determined without knowing the absolute number densities of the electronically excited levels, which are most likely in non-equilibrium.

The assumed heat shield stagnation point temperatures, which produced the best fitting spectra, are considered to be the effective rotational and vibrational temperatures. Temperature gradients have been neglected in this process. The agreement between this simulation and experimental data is satisfactory, see Figure 15. At high altitudes, strong scattering is seen in the data, which may result from the emission of molecules or atoms not yet identified.

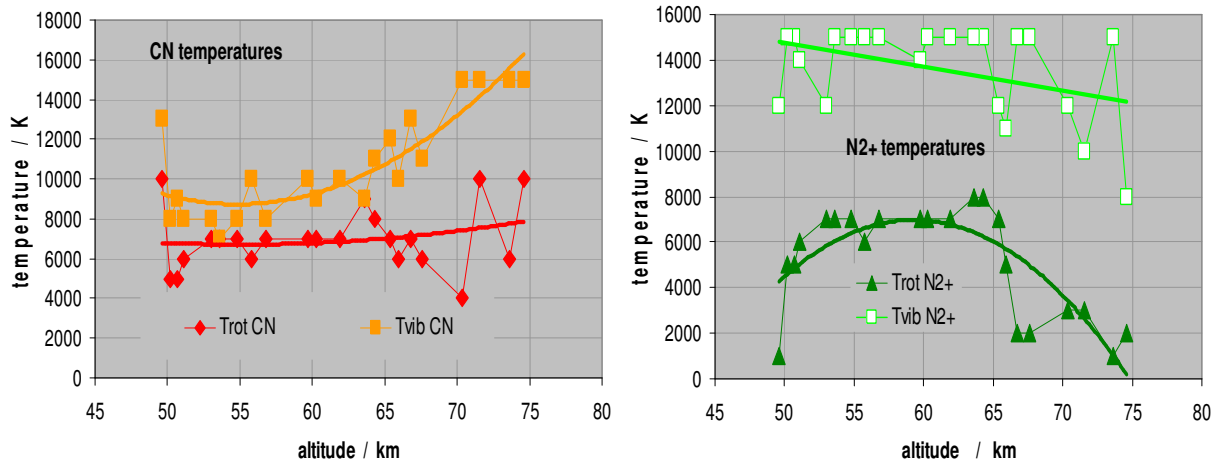


**Figure 13: Vibrational and rotational temperatures of CN and  $N_2^+$  along STARDUST trajectory**

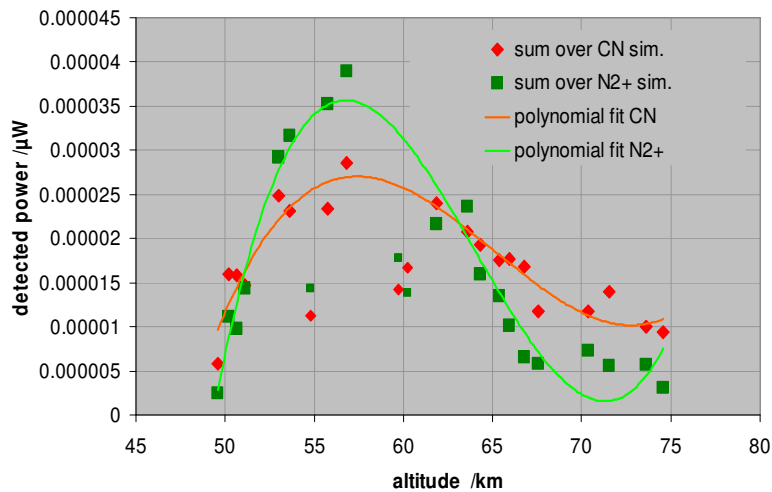


**Figure 14: Radiant power of 1<sup>st</sup> neg. systems of CN and  $N_2^+$  along STARDUST trajectory**

Evaluating spectra for several altitudes one obtains the species' temperature profile along the trajectory.  $N_2^+$  and CN show different temperature histories, see Figure 13. CN is produced near the surface with thus depending on the surface temperature, while  $N_2^+$  is formed mainly in the post shock layer. The vibrational temperature of CN is generally lower than that of  $N_2^+$ . For  $N_2^+$  the highest simulation temperature of 15000 K was too low, though. At altitudes below 67 km rotational temperatures of CN and  $N_2^+$  are similar. Using these temperatures and the fit to the spectra, the detected radiant power caused by the 1<sup>st</sup> neg. systems of CN and  $N_2^+$  was computed as the integrated value of the simulated spectra, see Figure 14.

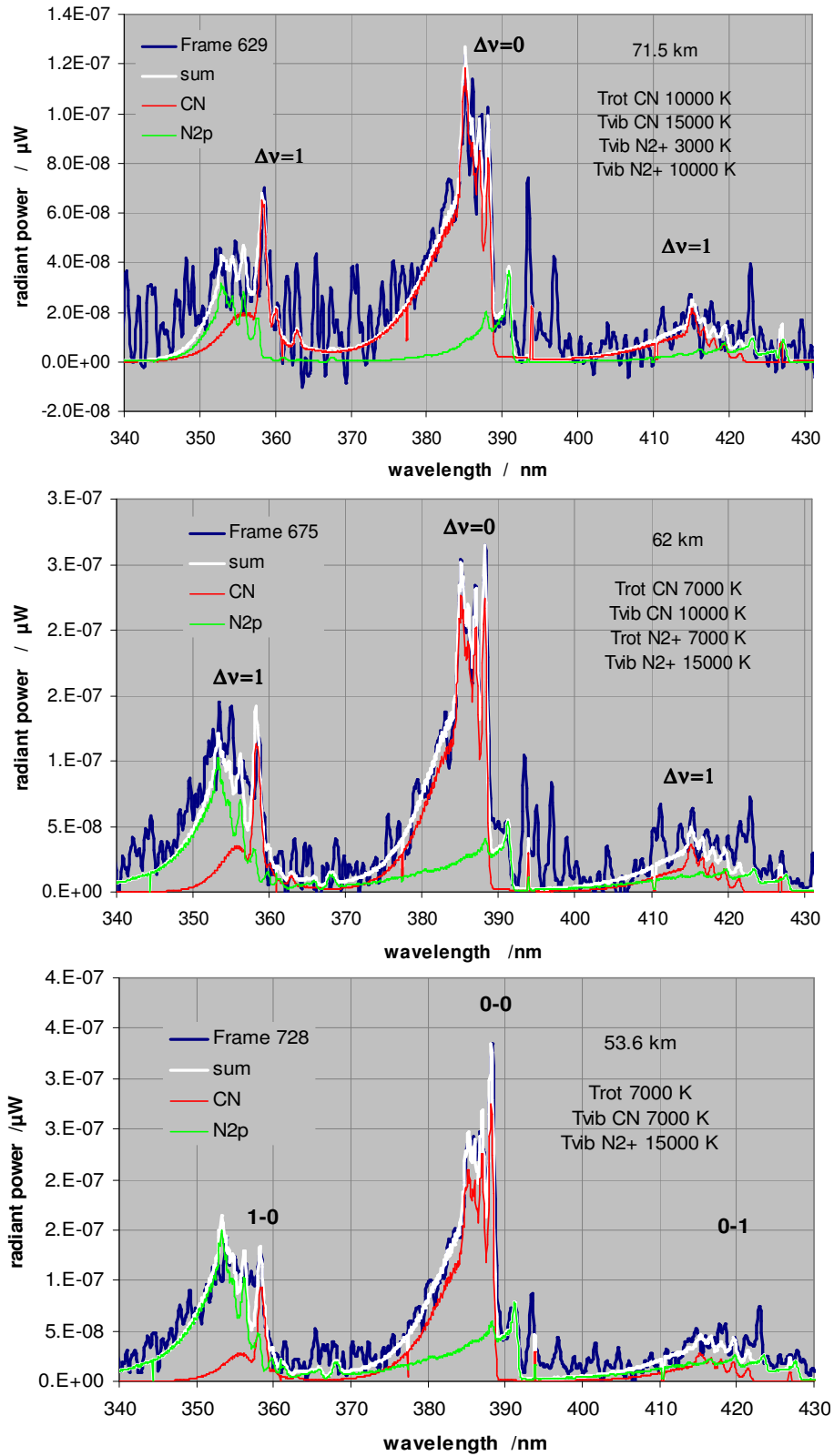


**Figure 15: Emission spectra of CN and N<sub>2</sub><sup>+</sup> ( $\Delta v = 0$ ,  $\Delta v = 1$ ,  $\Delta v = -1$  bands) at 71.5 km, 62 km and 53.6 km of altitude: Experimental data (blue) and simulation results (white)**

A spectral simulation with PARADE [12] based on URANUS [15] computations of the flow field around Stardust did not show satisfying results, though. This is mainly due to the fact that the two strongest radiators CN and  $N_2^+$  are not present in the flow field solver or exist in very low concentrations only. Recent publications such as ref. [14] predict plasma properties which might be the basis for a more accurate data evaluation.

## 5.0 PWT conditions for STARDUST rebuilding

The IRS plasma wind tunnel PWK1 will be used in combination with the magnetoplasmadynamic generator RD5.

### Plasma Source and Plasma Wind Tunnel for the rebuilding of the STARDUST re-entry

Five plasma wind tunnels (PWK 1 - 5) are in operation at IRS for the investigation and qualification of TPS materials [3]. The vacuum tank used for PWK 1 is a 6 m steel tank with a diameter of 2 m and double-wall cooling. The tank is equipped with a 4-axis positioning system on which the different probes and the specimen support system can be mounted. This allows the simulation of parts of the re-entry trajectories by moving the specimen in different plasma flow regimes. A trajectory point is defined by the ambient pressure, the axial distance to the generator, the arc current and the mass flow. These values result in the proper enthalpy, total pressure and temperature or heat flux.

Different plasma sources have been developed for generating the high enthalpy plasma flows expected for re-entry flights. In the magnetoplasmadynamic generator (MPG) RD5, the test gas is heated by means of an electric arc and electromagnetic forces are used for acceleration.

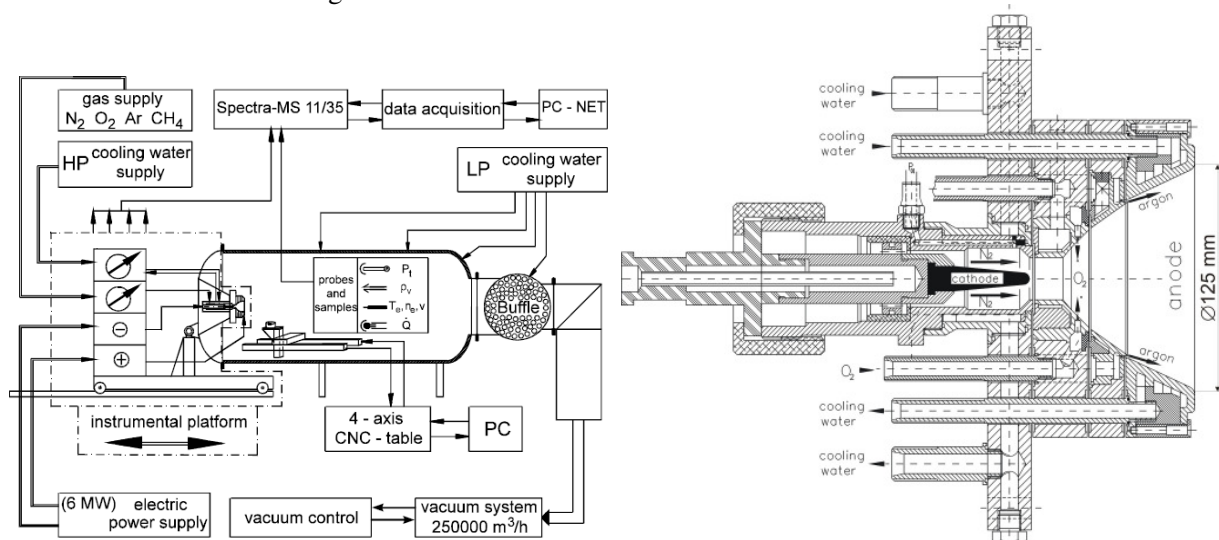


Figure 16: IRS Plasma wind tunnel PWK1 and MPG RD5

### Heat flux measurements

At IRS stationary heat flux is often measured using water cooled calorimeters which are geometrically very similar to the material samples used and their support system. The calorimeter inlet area, which is exposed to the plasma, is similar to the area of the tested specimens.

For steady state heat flux measurements the flow rate and the temperature difference of the incoming and outgoing water is measured using thermocouples of type K, which are coated in order to avoid any influence by the plasma potential.

The heat flux per unit area is

$$\dot{q}_{Cu} = \frac{\dot{m}_w c_{p,w}(T, p)(\tau_{w,out} - \tau_{w,in})}{A}$$

With the water mass flow rate

$$\dot{m}_w = \dot{V}_w \rho_w(T, p)$$

The density  $\rho_w$  and the heat capacity  $c_{p,w}$  of water are estimated for a pressure  $p$  of 1 MPa. The temperature  $T$  for the estimation of  $c_{p,w}$  is the arithmetic average of the temperature of the outgoing water  $\tau_{w,out}$  and of the incoming water  $\tau_{w,in}$ . For the density the temperature of the outlet is used because the volume flow is measured by a water flow meter in the outlet of the water circuit.

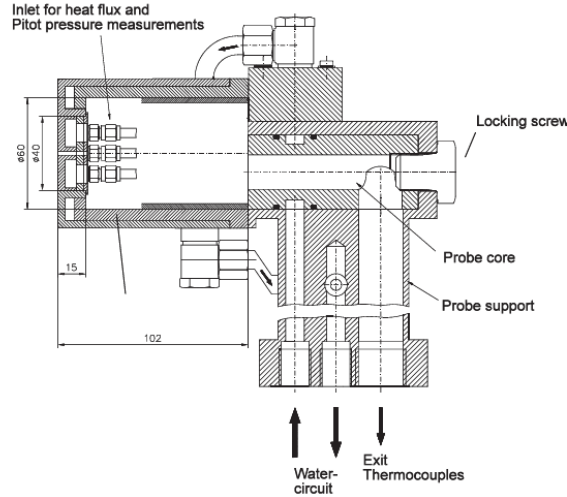


**Figure 17: Double probe for calorimetric and total pressure measurements**

For the enthalpy calculation, the flow rate of the incoming water of the thruster anode is measured. The flow rate of each segment of the thruster is calculated by previously measured correlation factors. Water temperatures are measured for each segment. Since the power input of the MPG is known by the measured product of current and voltage, the effective enthalpy of the plasma jet at the end of the nozzle exit is easily obtained by the difference between the electric power input  $P_{el}$  and the total heat loss  $Q'$

$$\bar{h}_{nz} = \frac{P_{el} - \sum_{i=1}^n \dot{Q}_{w,i}}{\dot{m}_{tot}} = \frac{U \cdot I - \sum_{i=1}^n \dot{m}_{w,i} \cdot c_{p,w} \cdot (\tau_{w,out,i} - \tau_{w,in,i})}{\dot{m}_{tot}}$$

This relation does not account for any inhomogeneous heating and acceleration processes in the nozzle and the combustion chamber. Thus, the calculated enthalpy and the enthalpy locally in the free stream are usually different. To investigate the local specific enthalpy in the freestream plasma, the relation of MARVIN and POPE may be used

$$\dot{q}_{fc} = K \cdot \left( \frac{p_{tot}}{r_{eff}} \right)^{1/2} \cdot h_{t,e},$$

with  $K = 117 \text{ kW}/(\text{m}^{3/2} \text{ atm}^{1/2} \text{ MJ/kg})$  for air,  $h_{t,e}$  the freestream enthalpy and  $r_{eff}$  being an effective probe nose radius

$$r_{eff} \approx 2.7 \cdot r_f$$

for a flat-faced probe with radius  $r_f$ . The local specific enthalpy and the actual heat flux onto the surface of a hot specimen can also be estimated by using a similar equation

$$\dot{q}_{cw} = K \cdot \left( \frac{p_{tot}}{R_{eff}} \right)^{1/2} \cdot (h_{tot} - h_{cw})$$

With  $q'_{c,w}$  being the measured cold wall heat flux on copper,  $h_{tot}$  the local specific enthalpy and  $h_{c,w}$  the cold wall enthalpy assumed to be 0.4 MJ/kg. Usually, the cold wall enthalpy is neglected.

Several measurements were conducted in order to reproduce the heat flux of the STARDUST capsule at peak heating of approximately 12 MW/m<sup>2</sup>, see also Fig. 1. At constant MPG current the probe was moved along the axis of the tank towards the nozzle, see Figure 18 (left).

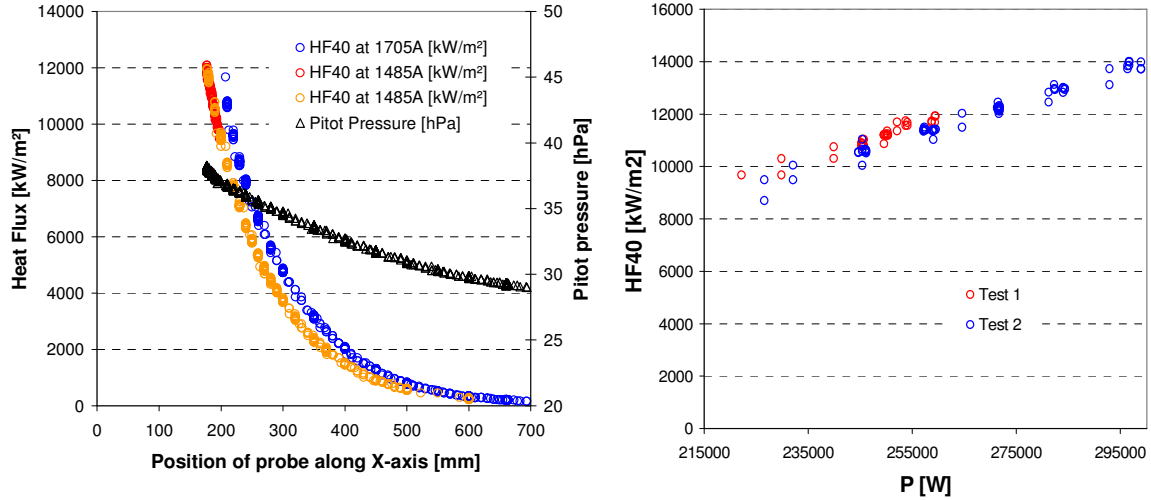


**Figure 18: Heat flux and Pitot pressure along PWK1 x-axis (left) and heat flux per power at MPG**

At 1483 A current (147 V) a maximum heat flux of 12.1 MW was reached at 177 mm from the nozzle at an ambient pressure of 27 hPa and a total pressure of 38 hPa, using a mass flux of 18.55 g/s of air (13.85 g/s N<sub>2</sub>, 4.21 g/s O<sub>2</sub>, 0.49 g/s Ar). Keeping the distance to the nozzle constant at 197 mm and increasing the MPG's power output to up to 297 kW, heat fluxes up to 14 MW/m<sup>2</sup> were produced at a total pressure of 38.7 hPa, as shown in Figure 18 (left). Thus, STARDUST heat fluxes at peak heating were successfully reproduced.

## 6.0 Conclusions

The emission of post shock and surface radiation for the STARDUST re-entry was observed. Spectra were taken from 324 nm to 456 nm with a pixel resolution of 0.08 nm and a measurement frequency of 5 Hz during 30 s around the point of maximum heating. The emission of CN as a major erosion product as well as N<sub>2</sub><sup>+</sup> and different atoms were confirmed. All measurement data represent an integration both over the visible part of the heat shield and the plasma in the post shock region. The measured spectra were split into continuum spectra and the line spectra of the plasma in the post shock layer. Scattering during the calibration measurements was observed and corrected for plasma emission via recalibration. Planck temperatures were found assuming a linear temperature distribution along the heat shield. The distance of STARDUST to DC8, orientation (viewing factors) and atmospheric transmission were taken into account. A peak temperature of 2850 K at 62 km altitude was found. Scattered light due to thermal radiation above 500 nm was taken into account for each spectrum separately. Contributions of dust particles in the plasma have not been taken into account. Rotational and vibrational temperatures of CN and N<sub>2</sub><sup>+</sup> were estimated using a comparison to numerically simulated spectra. Plasma temperature gradients and composition gradients across the post shock layer were neglected because of the unavailability of flow field data. Furthermore, plasma conditions for STARDUST rebuilding have been identified and STARDUST heat fluxes at peak heating were successfully reproduced during plasma wind tunnel experiments, reaching heat fluxes of up to 14 MW/m<sup>2</sup>.



References:

- <sup>1</sup> “Stardust Hypervelocity Entry Observing Campaign Support”, NASA Engineering and Safety Center Report, RP-06-80, August 31, 2006
- <sup>2</sup> Winter, M., Herdrich, G., „Heat Shield Temperatures and Plasma Radiation obtained from Spectroscopic Observation of the STARDUST Re-Entry in the Near UV”, 46th AIAA Aerospace Sciences Meeting and Exhibit, Reno, Nevada, Jan. 7-10, 2008, AIAA-2008-1212
- <sup>3</sup> Herdrich, G., Auweter-Kurtz, M., Endlich, P., Kurtz, H., Laux, T., Löhle, S., Nazina, N., Pidan, S., Schreiber, E., Wegman, T. and Winter, M., „Atmospheric Entry Simulation Capabilities at IRS,“ 3rd International Symposium on Atmospheric Reentry vehicles and systems, Arcachon, France, March 2003
- <sup>4</sup> Winter, M., “Emission Spectroscopic Investigation of the Flow Field around a Blunt Body in a High Enthalpy Flow”, Dissertation (in German), Institut für Raumfahrtssysteme, Universität Stuttgart, Germany, 2006
- <sup>5</sup> Röck, W., “Simulation des Eintritts einer Sonde in die Atmosphäre des Saturnmondes Titan in einem Plasmawindkanal”, Dissertation (in German), Institut für Raumfahrtssysteme, Stuttgart, Germany, 1999
- <sup>6</sup> Desai, P.N.; Mitcheltree, R.A.; Cheatwood, F. McNeil: “Entry Trajectory Issues for the Stardust Sample Return Capsule”, International Symposium on Atmospheric Reentry Vehicles and Systems, Arcachon, France, March 16-18, 1999.
- <sup>7</sup> Jenniskens P., Kontinos D., Jordan D., Wright M., Olejniczak J., Raiche G., Wercinski P., Desai P.N., Taylor M.J., Stenbaek-Nielsen H.C., McHarg M.G., Abe S., Rairden R.L., Albers J., Winter M., Harms F., Wolf J., ReVelle D.O., Gural P., Dantowitz R., Rietmeijer F., Hladiuk D., Hildebrand A.R. Preparing for the meteoric return of Stardust. Workshop on Dust in Planetary Systems (ESA SP-643). 26-30 September 2005, Kauai, Hawaii.
- <sup>8</sup> Jenniskens, P.; Jordan, D.; Kontinos, D.; Wright, M.; Olejniczak, J.; Raiche, G.; Wercinski, P.; Schilling, E.; Taylor, M.; Rairden, R.; Stenbaek-Nielsen, H.; McHarg, M.G.; Abe, S.; Winter, M. Preliminary Results From Observing The Fast Stardust Sample Return Capsule Entry In Earth's Atmosphere On January 15, 2006, Progress in Planetary Exploration Missions, 26th meeting of the IAU, Joint Discussion 10, 21-22 August 2006, Prague, Czech Republic
- <sup>9</sup> Bernstein, L.S., A. Berk, P.K. Acharya, D.C. Robertson, G.P. Anderson, J.H. Chetwynd and L.M. Kimball, Very Narrow Band Model Calculations of Atmospheric Fluxes and Cooling Rates, Journal of Atmospheric Sciences, Vol. 53, No. 19, pp. 2887-2904 (1996).
- <sup>10</sup> <http://es-ee.tor.ec.gc.ca/cgi-bin/selectMap?lang=e&type1=du&day1=10&month1=01&year1=2006&howmany1=10&interval1=1&intervalunit1=d&hem1=n&type2=no&day2=19&month2=07&year2=2006&howmany2=1&interval2=1&intervalunit2=d&hem2=n&mapsize=100>
- <sup>11</sup> Huy K. Tran, Christine E. Johnson, Daniel J. Rasky and Frank C. Hui, Ames Research Center, Moffet Field, California; Ming-Ta Hsu, Tomothy Chen and H.C. Chem, San Jose, California; Y.K. Chen, Thermosciences Institute, Moffet Field, California; Daniel Paragas and Loreeen Kobayashi, Foothill-De Anza College, Cupertino, California: Pheonlic Impregnated Carbon Ablators (PICA) as Thermal Protection Systems for Discovery Missions, NASA Technical Memorandum 110440, Ames Resaerch Center, Moffett Field, California 94035-1000, April 1997.
- <sup>12</sup> Winter, M., Pfeiffer, B., Fertig, M., Auweter-Kurtz, M., Smith, A. J.: Recent Status of the Plasma Radiation Database PARADE, AIAA-2004-2376, AIAA Thermophysics Conference, USA, Portland, Oregon, 2004.
- <sup>13</sup> Fertig, M., Dohr, A., Frühauf, H.-H.: Transport Coefficients for High Temperature Nonequilibrium Air Flows, AIAA Journal of Thermophysics and Heat Transfer, Vol.15, No.2, 2001.
- <sup>14</sup> T. Ozawa, J. Zhong, D. A. Levin, D. Bogerz and M. Wright: Modeling of the Stardust Reentry Flows with Ionization in DSMC, 45th AIAA Aerospace Sciences Meeting and Exhibit, 9-12 January 2007, Reno, NV
- <sup>15</sup> Fertig, M., Dohr, A., Frühauf, H.-H.: Transport Coefficients for High Temperature Nonequilibrium Air Flows, AIAA Journal of Thermophysics and Heat Transfer, Vol.15, No.2, 2001.